Check for updates

View Article Online
View Journal

Nanoscale

Accepted Manuscript

This article can be cited before page numbers have been issued, to do this please use: J. Xu, M. Fu, Y. Xu, J. Xu, X. Xiao, Q. Zhang, Y. Lu, K. Evers, C. Liu, S. A. Maier, R. Oulton, M. P. Ryan and F. Xie, *Nanoscale*, 2026, DOI: 10.1039/D6NR00068A.

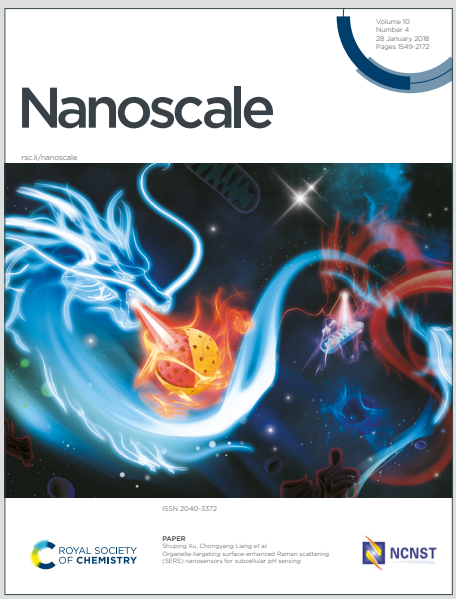

This is an Accepted Manuscript, which has been through the Royal Society of Chemistry peer review process and has been accepted for publication.

Accepted Manuscripts are published online shortly after acceptance, before technical editing, formatting and proof reading. Using this free service, authors can make their results available to the community, in citable form, before we publish the edited article. We will replace this Accepted Manuscript with the edited and formatted Advance Article as soon as it is available.

You can find more information about Accepted Manuscripts in the Information for Authors.

Please note that technical editing may introduce minor changes to the text and/or graphics, which may alter content. The journal's standard Terms & Conditions and the Ethical guidelines still apply. In no event shall the Royal Society of Chemistry be held responsible for any errors or omissions in this Accepted Manuscript or any consequences arising from the use of any information it contains.

ROYAL SOCIETY OF CHEMISTRY

rsc.li/nanoscale

View Article Online
DOI: 10.1039/D6NR00068A

Boosting NIR-I Luminescence of Lanthanide Nanoparticles Excited in NIR-II by Plasmonic Arrays

Authorship: Jiamin Xu, Fu Ming, Yunfan Xu, Jingdong Xu, Xiaofei Xiao, Qiyu Zhang, Yao Lu, Koen Evers, Changxu Liu, Stefan Maier, Rupert Oulton, Mary Ryan, Fang Xie

Open Access Article. Published on 13 April 2026. Downloaded on 4/14/2026 3:06:13 PM.
This article is licensed under a Creative Commons Attribution 3.0 Unported Licence.

Nanoscale Accepted Manuscript

Abstract

The exploitation of lanthanide-induced NIR luminescence holds significant potential for advancing biosensing and imaging technologies, because of its deeper imaging penetration depth and lower biosensing noise than visible light. However, the low quantum efficiency of light generation, along with the high cost and poor sensitivity of light detection for NIR-II photons, have largely constrained the application of NIR-II luminescence for bio-imaging and sensing. To overcome these challenges, we have developed a new strategy for NIR bioimaging and sensing, by using Tm^{3+} doped $NaYF_4$ upconversion nanoparticles (UCNPs) which emit NIR-I upconversion luminescence (UCL) at 808 nm under NIR-II excitation at 1208 nm. The 1208 nm excitation enables deeper imaging penetration due to negligible autofluorescence, thereby reducing biosensing noise, resulting in an enhanced signal-to-noise ratio (S/N) from a minimal noise background. Meanwhile, the NIR-I emission at 808 nm allows deep tissue penetration, while allowing highly sensitive detection of NIR-I photons using conventional detectors, which are much more accessible than NIR-II detection systems. The intrinsically weak NIR UCL signals were further amplified by up to 210-fold using a pioneering plasmonic approach, achieved by coupling UCNPs with a periodic silver hole-cap nanoarrays (Ag-HCNA). Three-dimensional finite-difference time-domain (3D-FDTD) simulations and lifetime analyses revealed substantial electric field enhancements under 1208 nm excitation and accelerated radiative decay at 808 nm, contributing to both excitation and emission enhancement. The potential use of Ag-HCNA-UCNP conjugates for fluorescence immunoassay platforms was further validated by immobilizing streptavidin-functionalized UCNPs (SA-UCNPs) onto biotinylated Bovine Serum Albumin (bBSA)-pre-grafted substrates, resulting in up to a 113-fold increase in UCL intensity. This plasmonic-enhanced UCL platform offers significant advantages, including cost-effective detection of 808 nm emission using silicon-based detectors, improved signal-to-noise ratio through enhanced tissue penetration, and reduced autofluorescence enabled by NIR-II excitation.

Introduction

Fluorescence-based technologies within the visible (400–700 nm) and the first near-infrared (NIR-I, 700-900 nm) regions have been extensively explored for biomedical applications over the past decades [1],[2],[3]. However, these spectral regions suffer from significant limitations due to photon

View Article Online
DOI: 10.1039/D6NR00068A

absorption by biological media, such as water, haemoglobin, lipids, and melanin, as well as substantial photon scattering within biological tissues, leading to severe interference from biological tissue autofluorescence in the visible range [4],[5]. Although NIR-I wavelengths partially mitigate these issues by reducing autofluorescence and enabling deeper tissue penetration, further improvements are required for high-performance biomedical applications [6],[7].

In contrast, the second near-infrared window (NIR-II, 1000–1700 nm) exhibits outstanding capabilities, including deeper tissue penetration, minimal tissue scattering, negligible autofluorescence, and superior temporal and spatial resolution [8],[9]. To fully harness the potential of NIR-II fluorescence for advanced biomedical imaging and biosensing, the development of efficient and stable fluorescent nanoprobes is essential.

Among the available nanoprobes such as small-molecule dyes [10],[11], quantum dots (QDs)[12], [13] and single-walled carbon nanotubes (SWCNTs)[14],[15], lanthanide-doped nanoparticles (LDNPs) have attracted particular interest due to their unique luminescent properties [16],[17]. These include large Stokes or anti-Stokes shifts, robust photostability, long luminescence lifetimes, and low cytotoxicity [17]. Such intrinsic characteristics render LDNPs promising candidates for a broad range of applications, ranging from *in vitro* bioassays to *in vivo* imaging, positioning them as one of the most promising candidates in the field of nanobiotechnology[16],[18].

LDNPs can emit both upconversion luminescence (UCL) and downconversion luminescence (DCL) according to their luminescence pathways [19]. UCL is an anti-Stokes process [20],[21]. This involves the successive absorption of two or more lower-energy photons in the NIR-I/NIR-II regions, followed by the emission of one higher-energy photon, typically in the visible region. In contrast, DCL is a Stokes process, where a photon is absorbed and converted into a photon with lower energy. LDNPs typically consist of a host matrix that incorporates sensitizer and emitter ions such as Yb^{3+}, Er^{3+}, Nd^{3+}, and Tm^{3+}, enabling emission across the visible to NIR-II regions under NIR-II excitation [18],[22]. Various host matrix materials with asymmetric crystalline structures have been successful in producing LDNPs with detectable UCL or DCL signals, including fluoride-based hosts [23],[24],[25], and oxide-based hosts [26],[27]. Among these, fluoride hosts, particularly $NaLnF_4$, are preferred due to their low phonon energies and high photochemical stability, which improve the efficiency of lanthanide-ion-induced luminescence [28],[29]. Previous studies have reported various types of UCL-emitting LDNPs, commonly termed upconversion nanoparticles (UCNPs), which are frequently excited in the NIR-II region to maximise tissue penetration [22],[30]. However, UCL processes suffer from intrinsically low quantum efficiencies, and their visible emissions are prone to re-absorption by biological tissues, limiting detection sensitivity [31].

Open Access Article. Published on 13 April 2026. Downloaded on 4/14/2026 3:06:13 PM.
This article is licensed under a Creative Commons Attribution 3.0 Unported Licence.

Nanoscale Accepted Manuscript

View Article Online
DOI: 10.1039/D6NR00068A

Open Access Article. Published on 13 April 2026. Downloaded on 4/14/2026 3:06:13 PM.
This article is licensed under a Creative Commons Attribution 3.0 Unported Licence.

Nanoscale Accepted Manuscript

In contrast, a class of LDNPs that emit photons at lower energy than the excitation source is termed downconversion nanoparticles (DCNPs). These are engineered to optimize both excitation and emission wavelengths within the NIR-II region, which can enhance tissue penetration and reduce autofluorescence, making them highly attractive for biological applications. Recent studies have demonstrated that NIR-II emitting DCNPs can overcome key limitations of conventional fluorescence immunoassays by reducing background interference and lowering the limit of detection (LOD) [41],[42],[43]. Such NIR-II emitting immunoassay nanoplatforms therefore offer enhanced sensitivity and improved accuracy.

Nevertheless, the practical application of LDNPs remains limited by inherently low NIR quantum yields (typically 0.1-3%) [18],[22],[32]. Furthermore, detection of NIR-II photons requires indium gallium arsenide (InGaAs)-based CCD cameras, which are significantly more expensive than conventional Si-based CCD cameras (suitable for NIR-I photons but unsuitable for NIR-II photons). Since NIR-II detectors are deemed too expensive for broad clinical use [9],[33], the high cost of essential instrumentation presents another major barrier to widespread adoption.

To address these limitations, there is a pressing need to develop a new class of LDNPs that combine the advantages of traditional UCNPs and DCNPs. Ideally, such systems would be excited in the NIR-II region and emit in the NIR-I region, enabling deep tissue penetration, low autofluorescence, and detection with cost-effective Si-based CCD cameras, thereby expanding their applications in bioimaging and biosensing. Moreover, the quantum efficiency of these nanoparticles should be enhanced to match or surpass that of commercial fluorophores.

One promising strategy to overcome the low quantum efficiency of LDNPs is Metal-enhanced fluorescence (MEF), also known as plasmonic enhanced fluorescence. MEF exploits surface plasmon resonance (SPR) in metallic nanostructures to modify the excitation and emission dynamics of nearby fluorophores, leading to significant fluorescence amplification [34],[35],[36]. Periodic noble metal nanoarrays with sharp SPR features have emerged as promising nanoplatforms for MEF [37], [38]. Among fabrication approaches, colloidal lithography offers a scalable and cost-effective route to fabricate noble metal periodic nanoarrays, such as gold nanohole arrays [39], silver nanotriangular arrays [40], and gold hole-cap arrays [28]. These two-dimensional (2D) and three-dimensional (3D) nanoarray architectures enable precise spectral tuning for optimal plasmonic coupling to amplify the weak emission of LDNPs.

In this work, we report a novel type of $NaYF_4$ UCNP solely doped with Tm^{3+} ions, capable of emitting NIR-I photons at 808 nm under 1208 nm NIR-II laser excitation. Upon coupling these UCNPs with Ag hole-cap coupled nanoarrays (Ag-HCNA), a remarkable enhancement exceeding 210-fold in UCL intensity was achieved. The three-dimensional Ag-HCNAs were fabricated via colloidal lithography, as

View Article Online
DOI: 10.1039/D6NR00068A

illustrated in Scheme 1, where a self-assembled film of polystyrene (PS) spheres was oxygen plasma-etched to facilitate the deposition of a thin Ag layer not only in the gaps between adjacent oval-shaped PS spheres but also on their upper hemispheres. Furthermore, the applicability of this plasmonic platform for accessible fluorescence immunoassays was validated by immobilizing a sub-monolayer of streptavidin-functionalized UCNPs (SA-UCNPs) on bBSA pre-grafted Ag-HCNA substrates. An enhancement of up to 113-fold relative to glass substrates was obtained, demonstrating the strong potential of this system to significantly amplify weak NIR-UCL signals in plasmonic-enhanced UCL immunoassays used for biosensing.

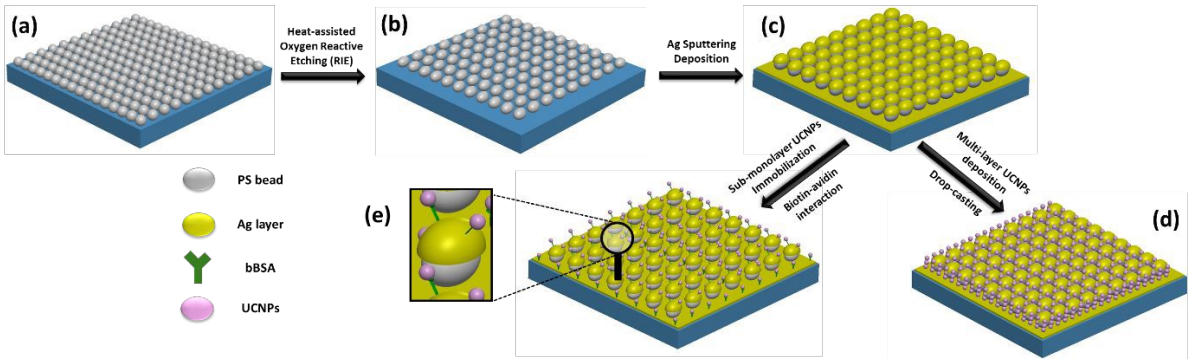

Scheme 1. Schematic illustration of the workflow for Plasmonic-enhanced UCL on Ag-HCNA films: (a) Self-assembled PS beads on glass substrate (b) Formation of self-assembled shrunk PS beads via RIE, (c) Creation of Ag-HCNA film through Ag sputtering, (d) Deposition of multi-layer Tm^{3+}-doped UCNPs onto Ag-HCNA via drop-casting, (e) Immobilization of a sub-monolayer of DCNPs onto the Ag-HCNA film through biotin-avidin interaction.

Experimental Section

Chemicals and materials: Sodium hydroxide (NaOH, ≥98%), thulium(III) acetate hydrate (99.9%), yttrium(III) acetate hydrate (99.9%), ammonium fluoride (NH_4F, 96%), cyclohexane (99.5%), oleic acid (OA, 90%), and 1-octadecene (ODE, 90%), poly(acrylic acid) (PAA), methanol (≥99.9%), silicon wafers, and sodium dodecyl sulfate (SDS, >99.0%), phosphate buffered saline (PBS), Streptavidin (from Streptomyces avidinii, affinity purified), 1-ethyl-3-(3-dimethylaminopropyl)carbodiimide, N-Hydroxysuccinimide (NHS), phosphate buffered saline (PBS, pH 7.4) and biotinylated bovine serum albumin (bBSA), were purchased from Sigma-Aldrich. Thiol-PEG-Amine, HCl salt (SH-PEG7500-NH_2, MW: 7500) was bought from JenKem Technology, Texas, USA. Monodisperse Polystyrene solution (5% w/v, 617 nm, and 418 nm) was purchased from Bangs Laboratories. All the chemicals were used without further purification.

Open Access Article. Published on 13 April 2026. Downloaded on 4/14/2026 3:06:13 PM.
This article is licensed under a Creative Commons Attribution 3.0 Unported Licence.

Nanoscale Accepted Manuscript

View Article Online
DOI: 10.1039/D6NR00068A

Synthesis of Tm^{3+} doped NaYF4 upconversion nanocrystals (UCNPs) Following a typical solvothermal method[23], 0.05 mmol of thulium(III) acetate hydrate and 0.95 mmol of yttrium (III) acetate hydrate powders were mixed in a three-neck round bottom flask. To this mixture, 7.5 ml of OA and 15 ml of ODE were then added with vigorous stirring. The mixture was heated to 145°C and maintained at that temperature for 1 h under vacuum until a transparent faint-yellow solution was obtained. After cooling the solution to 40°C, a mixture of 4 mmol of NH_4F and 2.5 mmol of NaOH dissolved in 10 ml of methanol was added. The resulting turbid solution was stirred vigorously at a temperature below 50°C for 30 min, followed by heating up to 120°C under vacuum to remove excessive water and methanol. Once no bubbles were observed, the orange solution was heated to 300°C under an argon atmosphere and maintained at that temperature for 90 min. After completion of the reaction, the solution was cooled to room temperature, and excess chemicals were washed several times with ethanol and acetone. The resulting pellet was finally redispersed in cyclohexane. Tm^3 doped $NaYF_4$ UCNPs with various Tm^{3+} doping concentrations were prepared by adjusting the molar ratio between thulium(III) acetate hydrate and yttrium(III) acetate, while keeping all other steps constant.

Preparation of PAA functionalized UCNPs (PAA-UCNPs)

The oleate ligands on the surface of DCNPs were initially eliminated through acid treatment [44]. Briefly, the cyclohexane-dispersed DCNPs were centrifuged and the collected yellow pellet was re-dispersed in 15 ml of ethanol, followed by adding 0.5 ml of HCl (0.1M) to adjust the solution pH to around 4. The turbid mixture was sonicated for 30 min at 40°C, followed by stirring at room temperature for 12 h. The obtained product was centrifuged and washed with water until neutral pH. To conjugate PAA onto the UCNPs, 2 mg/ml of PAA powder was added into 10 ml of aqueous UCNP solution. With rigorous stirring, NaOH (1M) solution was slowly dropped into the solution until pH 10-11. The solution was stirred at room temperature for 12 h. The obtained nanoparticles were collected by centrifugation at 10000 rpm for 15 minutes, washed multiple times with ethanol and water, and then redispersed in 10 ml of water. Finally, the nanoparticles were stored in a refrigerator at 4°C until used.

Streptavidin conjugation with PAA-UCNPs

Conjugation of streptavidin with PAA-UCNPs was achieved through EDC-NHS chemistry, following the reported method [45]. Briefly, PAA-UCNPs in 1 ml of MES buffer (50 mM, pH 6.0) were added to 0.4 mg of EDC and 0.6 mg of NHS. The solution was incubated on an orbital shaker for 30 min. After the reaction was complete, the solution was centrifuged at 10000 rpm for 30 min and the supernatant was discarded. The activated PAA-UCNPs was re-dispersed in 1 ml of PBS buffer (pH 7.4) containing 100µg/ml of streptavidin. The solution was then vortexed at room temperature for 4 h. The

Open Access Article. Published on 13 April 2026. Downloaded on 4/14/2026 3:06:13 PM.
This article is licensed under a Creative Commons Attribution 3.0 Unported Licence.

Nanoscale Accepted Manuscript

View Article Online
DOI: 10.1039/D6NR00068A

streptavidin conjugated UCNPs were collected by centrifugation at 4000 rpm for 20 min at 4°C and re-dispersed in 1 ml of PBS solution.

Fabrication of Ag-HCNA

The fabrication of Silver Hole-Cap Nanoarray film (Ag-HCNA) was followed a typical colloidal lithography method[28]. Initially, two types of polystyrene sphere (PS418 and PS617) formed their respective monolayer of closely-packed PS spheres in hexagonal arrangement onto glass slides through a previously reported self-assembled technique[46], [47]. The monolayer of PS spheres on the glass slide was treated by reactive ion etching (RIE) using O_2 for 50 s for PS418 and 40 s for PS617, respectively, with the same O_2 pressure of 20 Pa and O_2 flow rate of 20 sccm. Afterwards, a 40 nm thick layer of Ag was sputtered onto the etched PS sphere substrate using a Hex deposition system, with an argon flow rate of 10 sccm, a voltage of 630 V, and a current of 100 mA. The obtained substrate was placed on a hot plate at 90°C for 2 min and stored in a desiccator covered with aluminium foil until use.

Deposition of multilayered UCNPs onto Ag-HCNA

10 µl of SH-PEG7500-NH_2 in ethanol (10 µg/ml) was dropped onto both types of Ag-HCNA films, followed by incubating in a humidity condition for 30 min. The excess SH-PEG7500-NH_2 were rinsed off with ethanol. The as-prepared PAA-DCNP solution was diluted to around 50 µg/ml, followed by depositing 9 µL of DCNP solution onto the center of each type of PEGylated Ag-HCNA via drop-casting. The sample was placed under the fume hood for at least 30 min until the solvent was completely evaporated. As a reference, the same amount of DCNPs was deposited onto glass slide using the same drop-casting technique.

Immobilization of Streptavidin-functionalized UCNPs (SA-UCNPs) onto Ag-HCNA

The immobilization of SA-UCNPs onto Ag-HCNA was achieved through a Biotin-avidin interaction [45],[48]. Briefly, a solution containing 100 µg/ml of bBSA in PBS buffer (pH 7.4) was dropped onto the surface of Ag-HCNA, followed by incubation under a humidified environment for 2h. The excess bBSA molecules were then removed through rinsing with PBS buffer, and the sample was gently dried using N_2 gas. Subsequently, a solution containing 50 µg/ml of Streptavidin-DCNPs was dropped on the surface of bBSA-coated Ag-HCNA, and the sample was incubated under a humidified environment for 2h. Later, unbound SA-DCNPs were thoroughly rinsed off with PBS buffer, and the obtained SA-DCNPs immobilized Ag-HCNA was dried using N_2 gas. The fluorescence spectra were immediately measured. To assess the number of SA-DCNPs bound to Ag-HCNA, the fluorescence intensity of unbound nanoparticle was also measured. The number of bound SA-DCNPs were determined by subtracting fluorescence intensity of the total amount of SA-DCNPs from that of the unbound nanoparticles. As a control, an equivalent amount of SA-DCNPs was deposited onto bBSA coated glass. The average

Open Access Article. Published on 13 April 2026. Downloaded on 4/14/2026 3:06:13 PM.
This article is licensed under a Creative Commons Attribution 3.0 Unported Licence.

Nanoscale Accepted Manuscript

View Article Online
DOI: 10.1039/D6NR00068A

fluorescence enhancement factor was calculated based on $Enh_{total} = (I_{Ag} / I_{glass})(N_{glass} / N_{Ag})$, where I_{Ag} and I_{glass} represent the UCL intensity from DCNPs immobilized on Ag-HCNA and glass. N_{Ag} and N_{glass} represent the amount of DCNPs bound to Ag-HCNA and glass, respectively.

Characterization

The X-ray diffraction (XRD) profile of UCNPs were acquired by PANalytical. Cu Kα irradiation (k=1.5406 Å) was used as the X-ray source utilized, and the measurement spanned a range (2θ) spanned of 10° to 70° (2θ) with a step size of 0.0167°. The morphological features of UCNPs were characterized using a Jeol 2100F Transmission electron microscope (TEM), equipped with Energy-Dispersive X-ray Spectroscopy (EDX, Oxford Instruments, UK) at an accelerating voltage of 200 kV. Substrate samples were characterized by a Zeiss Auriga Scanning electron microscope (SEM) with an InLens detector at an acceleration voltage of 5 kV. The EDX (Oxford Instruments, UK) mode was performed at 20 kV. The extinction spectrum of samples were characterized using a UV-Vis-NIR spectrophotometer (Agilent Cary 5000). For the solution sample, a high-performance quartz cuvette was used, and the measurement was conducted from 700 nm to 1100 nm. The fluorescence intensity of aqueous UCNP samples with different Tm^{3+} doping concentrations was measured using a Fluorolog Tau3 system (Horiba Scientific) equipped with a PMT detector (700 nm to 900 nm) and an MDL-1028 nm continuous wave laser (500 mW, Changchun New Industries Optoelectronics Technology Co., Ltd.) to optimize the Tm^{3+} concentration. Fluorescence spectrum of substrate samples were obtained by Princeton Instruments Spec 10 system with a SP2300 equipped with A CW laser diode at a wavelength of 1208 nm. The excitation beam was incident perpendicularly onto the surface of the sample. The lifetimes of Tm^{3+} doped PAA-UCNPs on glass and Ag-HCNAs were characterized using a frequency domain lifetime measurement technique with modulated pump and detection methodology, while the Purcell factor simulations were conducted using the commercial FDTD software Lumerical Detailed methods for lifetime measurement and Purcell factor simulation are provided in the Supplementary documents, reported in our prior work [28],[49].

Result and Discussion

Synthesis of Tm^{3+} doped NaYF4 UCNPs

Open Access Article. Published on 13 April 2026. Downloaded on 4/14/2026 3:06:13 PM.
This article is licensed under a Creative Commons Attribution 3.0 Unported Licence.

Nanoscale Accepted Manuscript

View Article Online
DOI: 10.1039/D6NR00068A

Open Access Article. Published on 13 April 2026. Downloaded on 4/14/2026 3:06:13 PM.
This article is licensed under a Creative Commons Attribution 3.0 Unported Licence.

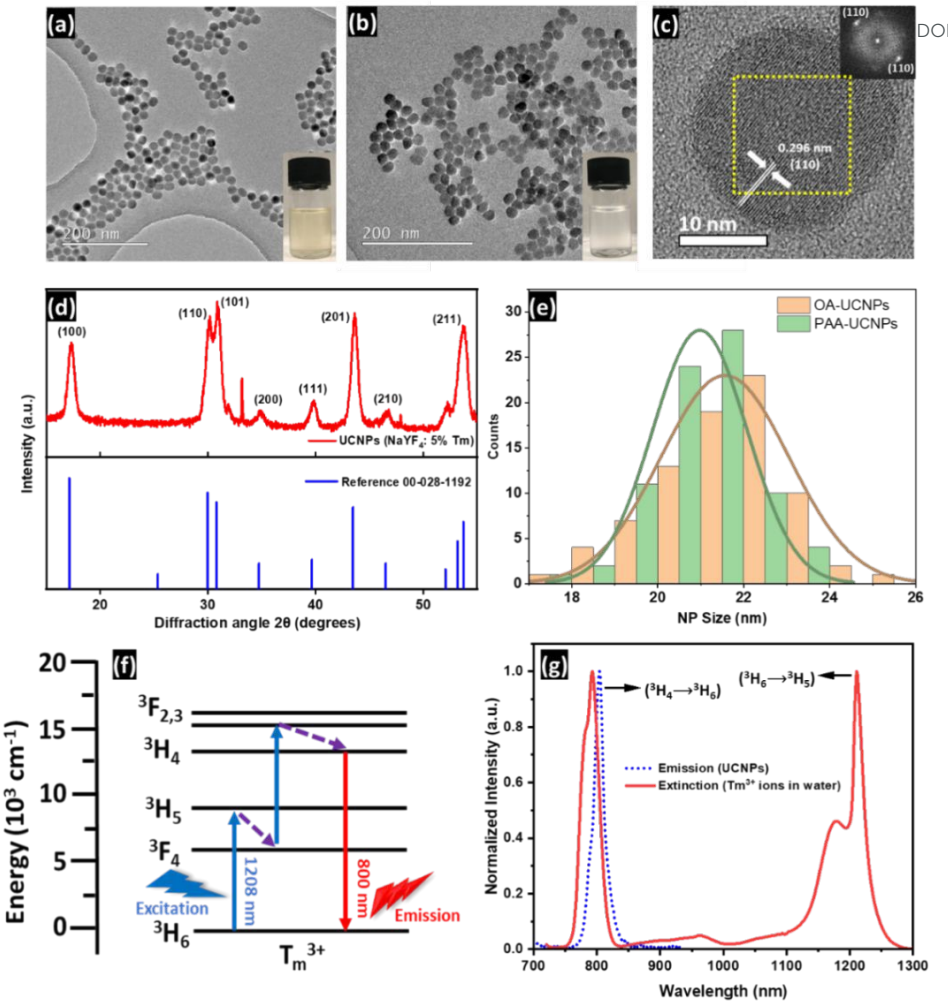

Figure 1 Characterizations of Tm^{3+} doped $NaYF_4$ UCNPs. (a-c) TEM images of (a) OA-capped UCNPs, (b) PAA-functionalized UCNPs, and (c) High-resolution TEM image of single PAA-functionalized UCNPs. Insets (a, b) digital camera images of OA-capped UCNPs dispersed in cyclohexane, and PAA-functionalized UCNPs in water. Inset (c) FFT pattern of the selected area within the yellow square. (d) XRD pattern of Tm doped $NaYF_4$ UCNPs dispersed on a wafer (red spectrum), and the Reference peaks of 00-028-1192 (blue vertical lines). (e) statistic size distributions of OA-capped UCNPs and PAA-functionalized UCNPs. (f) Energy transfer diagram within Tm doped $NaYF_4$ UCNPs under the excitation of 1208 nm. (g) the normalized extinction spectrum of Tm^{3+} ions in water (red spectrum), and the normalized NIR upconversion emission spectrum of aqueously-dispersed Tm doped $NaYF_4$ UCNPs under the excitation of 1208 nm.

Monodispersed $NaYF_4$: 5% Tm^{3+} UCNPs capped with oleate ligands were synthesized using a typical solvothermal method, as illustrated in Figure 1a. This Tm^{3+} concentration was optimized to achieve the highest UCL performance at 808 nm, as shown in Supplementary Figure 1. The capped oleate ligands are hydrophobic and are not biocompatible, hence a ligand exchange step was made by acid washing to remove oleate ligands and subsequently functionalized with PAA. Figure 2b and 2c shows the morphological features of PAA-

Nanoscale Accepted Manuscript

View Article Online
DOI: 10.1039/D0NR00068A

functionalized UCNPs under different magnitudes, and it was observed that the size, shape and uniformity of PAA-functionalized UCNPs underwent negligible changes compared to OA-capped UCNPs. Figure 2c shows that as-prepared $NaYF_4$: 5% Tm^{3+} UCNPs possess an average size of 21±3.1 nm with a narrow size distribution. Figure 1e shows the XRD pattern of PAA-functionalized $NaYF_4$: 5% Tm^{3+} UCNPs depositing onto Si wafer. It was noted that two line-like peaks at 33° and 48° denote the characteristic peaks of Si, while other characteristic peaks are well fitted to the hexagonal $NaYF_4$ crystalline structure indexed by Reference 00-028-1192. The lattice spacing of 0.296 nm measured from HR-TEM image (Figure 1c) corresponds to (110) facets of hexagonal $NaYF_4$, showing high alignment with XRD results.

Structural Design & Fabrication of Ag-HCNAs

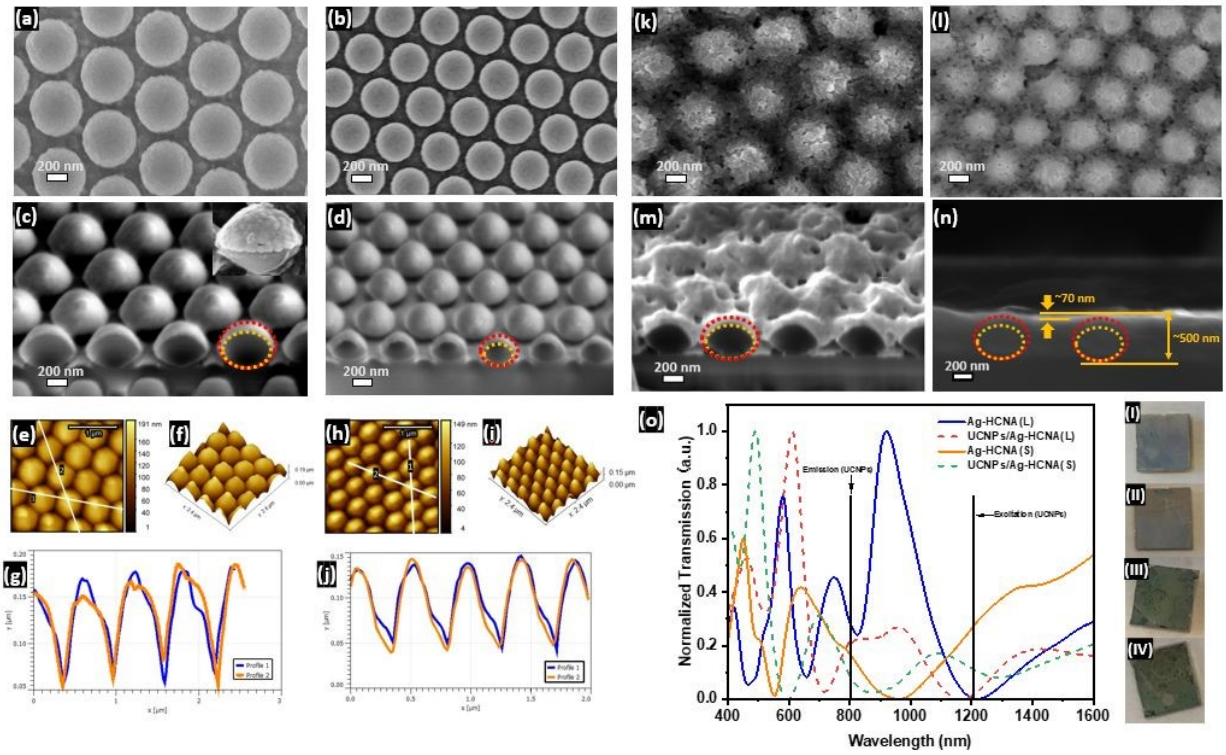

Figure 2 Morphological characterization of UCNPs coated Ag-HCNA films. (a, b) show SEM images of pristine (a) Ag-HCNA(L), and (b) Ag-HCNA(S) film. (c, d) show SEM-FIB images of (c) Ag-HCNA(L), and (d) Ag-HCNA(S) film, cutting through the middle of individual Ag hemisphere caps. Inset (c) shows SEM image of single Ag hemisphere cap. (e-h) show AFM topological images of (e) Ag-HCNA(L), and (h) Ag-HCNA(S) film. (f) and (i) show the 3D profiles corresponding to (e) and (h), respectively. (g) and (j) show the line profiles from labels in (e) and (h), respectively. (k, i) show SEM images of UCNPs coated PEGylated Ag-HCNA films, (k) UCNPs/Ag-HCNA(L); (i) UCNPs/Ag-HCNA(S). (m) shows SEM-FIB image of UCNPs/Ag-HCNA(L), cutting through the middle of individual Ag hemisphere caps. (n) shows SEM cross-sectional (90° tilting) image of UCNPs/Ag-HCNA(L). (o) shows transmission spectra of both types of Ag-HCNA films and the corresponding UCNPs/Ag-HCNA films. Insets (I-IV) show digital camera images of Ag-HCNA(L), UCNPs/Ag-HCNA(L), Ag-HCNA(S), UCNPs/Ag-HCNA(S) films, respectively. The yellow dotted line in (c), (d), (m), and (n) point out the oval shaped PS spheres, while each red dotted line point out the size of Ag hemisphere caps.

Open Access Article. Published on 13 April 2026. Downloaded on 4/14/2026 3:06:13 PM.
This article is licensed under a Creative Commons Attribution 3.0 Unported Licence.

Nanoscale Accepted Manuscript

View Article Online
DOI: 10.1039/D6NR00068A

Open Access Article. Published on 13 April 2026. Downloaded on 4/14/2026 3:06:13 PM.
This article is licensed under a Creative Commons Attribution 3.0 Unported Licence.

Nanoscale Accepted Manuscript

The morphological features of two types of Ag-HCNA films at different fabrication stages were characterized by SEM, as shown in Figure 2 a-d and Supplementary Figure 2 and 3. The structural parameters of films corresponding to each fabrication stage are summarized in Supplementary Table 1. Initially, the unetched PS-617 beads exhibited an average diameter of 617 ± 12 nm and a pitch size of ~610 ± 11 nm in the closely-packed PS film. After 50 s of oxygen plasma etching and subsequent Ag deposition, the PS beads transformed into an oval shape with reduced longitudinal and transverse dimensions of 494 ± 14nm and 384 ± 8 nm (Figure S2), respectively, while maintaining a largely unchanged pitch size (Supplementary Figure 3). The deformation from spherical shape to oval shape was induced by temperature gradients during plasma etching, as previously reported [50].Consequently, the subsequent Ag deposition resulted in Ag hemispherical caps with an average longitudinal diameter of ~530 ± 17 nm, an average separation distance of ~80 ± 7 nm between adjacent caps, and an estimated gap size of ~147 ± 8 nm (Figure 2 a, c). For PS-417 beads with 45 seconds of oxygen plasma etching and subsequent Ag deposition, the longitudinal and transverse dimensions were reduced to 348 ± 17 nm and 274 ± 10 nm, respectively, while the resultant gap size between the Ag hemispherical cap and the hole was estimated ~98 ± 10 nm. Notably, under these processing conditions, the separation distance between adjacent Ag hemispherical caps was adjusted to ~75 ± 11 nm, comparable to that achieved using PS-617 beads. These findings also imply the reproducibility and reliability of the obtained Ag-HCNA film using colloidal lithography nanofabrication method.

The deposition thickness of the Ag layer and the surface topographies of both types of Ag-HCNA films were further confirmed using AFM, as depicted in Figure 2 e-h and Supplementary Figure 6. Line profiles from the measured regions revealed a highly periodic arrangement of Ag hemispheres and holes, with an average Ag deposition thickness of approximately 50 nm across the scanned areas. These findings corroborate the observations obtained from SEM analysis.

Figure 2 k and I show the morphologies of UCNP-coated Ag-HCNAs. The thiol group from linear heterobifunctional SH-PEG-NH_2 ligands form a strong bond for the Ag-HCNA film, forming a dielectric spacer layer over 5 nm. This effectively minimized non-radiative energy transfer and quenching between the Ag surface and UCNPs. Besides, the amine groups on the opposite ends of the SH-PEG-NH_2 ligands served as anchoring sites for PAA-DCNPs and enhanced the hydrophilicity of PEGylated Ag-HCNA surface. To achieve a uniform coating and

View Article Online
DOI: 10.1039/D6NR00068A

facilitate systematic investigation of plasmonic modulations on UCNPs, PAA-UNCPs were directly deposited onto PEGylated Ag-HCNAs by drop-casting, forming an ~70 nm UCNPs layer on top of Ag-HCNAs (Figure 2 m, n). Notably, after coating with UCNPs, the structure and periodicity of the Ag-HCNAs remained largely unchanged.

Figure 2o shows the transmission spectra of two types of Ag-HCNAs before and after coating with DCNPs. The pristine Ag-HCNAs, for both types, exhibited multiple transmission peaks and dips across visible and NIR regions, attributed to the quadra-pole plasmonic modes arising from the structural elements such as the holes, caps, and their coupled features on the Ag-HCNA substrate. Upon coating with UCNPs, both types of Ag-HCNAs showed peak shifts and significant changes in their relative intensity between peaks in the visible and NIR regions. Since there was no evidence suggesting that UCNP deposition degrading the array's order, we assume that the peak shifts and intensity changes were primarily attributed to the changes in the dielectric environment. Importantly, after UCNP coating, the transmission dip of UCNPs/Ag-HCNA(L) closely matched extinction band of UCNPs at ~1208 nm, while UCNPs/Ag-HCNA(S) exhibited overlap with the emission band of UCNPs at ~808 nm. As the transmission dip likely corresponds to surface plasmon resonance of the nanostructured film, these strong spectral overlaps between Ag-HCNAs and the coupled UCNPs was expected to significantly enhance luminescence of UCNPs.

Luminescence Enhancement Results

Open Access Article. Published on 13 April 2026. Downloaded on 4/14/2026 3:06:13 PM.
This article is licensed under a Creative Commons Attribution 3.0 Unported Licence.

Nanoscale Accepted Manuscript

View Article Online
DOI: 10.1039/D6NR00068A

Open Access Article. Published on 13 April 2026. Downloaded on 4/14/2026 3:06:13 PM.
This article is licensed under a Creative Commons Attribution 3.0 Unported Licence.

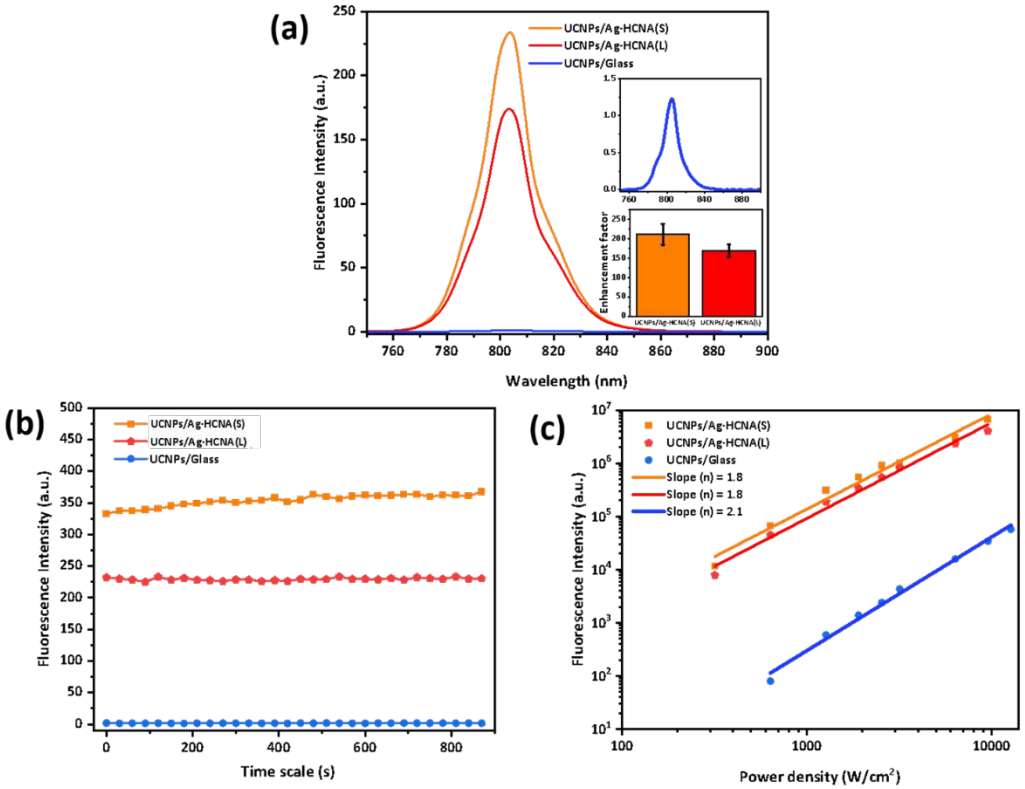

Figure 3 UCL enhancement study of UCNPs coated Ag-HCNA films, excited at 1208 nm. (a) PL spectra of UCNPs on glass slide and Ag-HCNA films. Inset: (upper) Zoomed-in image of PL spectra of UCNPs on glass slide; (bottom) Averaged fluorescence enhancement factor at the emission of 808 nm, calculated from the intensity ratio of UCNPs on Ag-HCNAs versus glass. (b) Fluorescence stability test. (c) Log-log plot of Power density versus fluorescence intensity of UCNPs on glass and on Ag-HCNAs.

The emission spectra of UCNPs on glass and on both types of Ag-HCNA films are shown in Figure 3a. The emission peak at ~808 nm corresponds to the electronic transition ($^3H_4 \longrightarrow {}^3H_6$) of Tm^{3+} ions within UCNPs excited at 1208 nm, consistent with the emission spectrum observed in their aqueous form (Figure 1g). Notably, a significant fluorescence enhancement was observed upon depositing UCNPs onto both types of Ag-HCNAs, with enhancements averaging 210-fold for Ag-HCNA(S), and 170-fold for Ag-HCNA(L), compared to UCNPs on glass.

Figure 3b shows the exceptional photostability of DCNPs on glass and on both types of Ag-HCNAs, even after long-time exposure to a NIR-II laser source. This was attributed to the intrinsic electronic configuration of emitter Tm^{3+} ions, wherein the electronic transitions of 4f electrons in Tm^{3+} ions are localized and negligibly affected by the surrounding environment due the shielding effect of the filled 5s and 5p sub-orbitals. The substantial enhancement of NIR UCL signals by Ag-HCNAs, upon excitation within the biologically transparent NIR-II window, combined with the demonstrated photostability,

Nanoscale Accepted Manuscript

View Article Online
DOI: 10.1039/D6NR00068A

implies the potential of integrating Ag-HCNAs with DCNPs as an ideal plasmonic platform for nanobiotechnology.

Figure 3c shows a log-log plot illustrating the corelation between fluorescence intensity of UCNPs and the excitation power on glass, Ag-HCNA (S), and Ag-HCNA(L) films. The fluorescence intensity demonstrated a nearly quadratic dependence on the excitation power density, indicative of a typical 'two-photon' luminescence process, where two photons from excitation source are absorbed and converted into a single higher-energy emitting photon[51]. This observation supports the proposed energy transfer mechanism depicted in Figure 1f.

Physical Mechanism Analysis

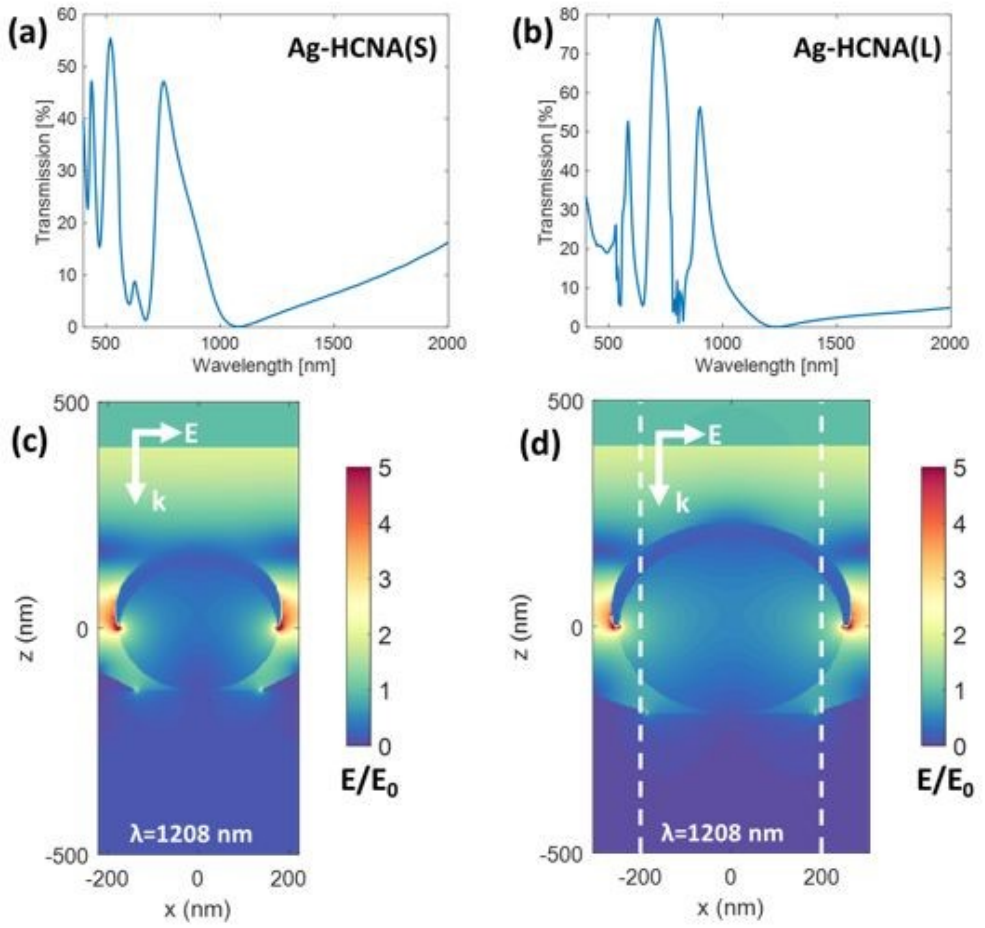

Figure 4: Simulation of Ag-HCNA(S) and Ag-HCNA(L) using 3D finite-difference time-domain (FDTD) method. (a, b) Simulated transmission spectrum for (a) Ag-HCNA(S) and (b) Ag-HCNA(L). (c, d) Local E-field enhancement plot under linear polarized 1208 nm excitation beam. The white dashed circle in (d) indicates the position along the x-axis, where x = ± 200 nm. 'E' represents the E-field polarization, and 'k' denotes the wave-vector. The unit bar in each E-field plot shows the amplitude of 'E'.

Open Access Article. Published on 13 April 2026. Downloaded on 4/14/2026 3:06:13 PM.
This article is licensed under a Creative Commons Attribution 3.0 Unported Licence.

Nanoscale Accepted Manuscript

View Article Online
DOI: 10.1039/D6NR00068A

Figure 4a and b present the simulated transmission spectra for Ag-HCNA(S) and Ag-HCNA(L), obtained using the three-dimensional finite-difference time-domain (FDTD) method with structural parameters from Supplementary Table 1. The simulated spectra exhibit several main peaks that closely match the experimental data shown in Figure 2o (blue and orange solid lines), indicating high periodicity and reproducibility for both array types. The excellent agreement in peak positions validates the accuracy of the structural modeling. However, minor discrepancies in intensity, such as near 800 nm, arise from factors not considered in the ideal simulation, including surface roughness and realistic metal loss.

Figure 4c and d show 3D FDTD modelling of the enhanced local E-field distribution across the surface of each Ag-HCNA type, under a 1208 nm linear polarized beam directed perpendicularly to the array surface. Notably, the local E-fields varied at different positions along the Ag-HCNA. For both types, the maximum local E-field enhancement of up to 5-fold was observed at the side edges of each hemispherical cap, while the regions between two adjacent hemispherical caps exhibited secondary strong local E-fields, varying from 3-fold to 5-fold enhancements. The excitation rate of Tm^{3+} ions within the UCNPs situated in these E-field-enhanced regions can be significantly accelerated, exhibiting a proportional relation with the degree of E-field enhancement, as described by Equation 1:

$$\frac{r}{r_0} \propto \left(\frac{E}{E_0}\right)^{2n} \quad (1)$$

Where 'r_0' and 'r' represent the original and accelerated excitation rates of sensitizer ions incorporated in UCNPs; 'E_0' and 'E' denote the magnitudes of the incident E-field and the enhanced local E-field, respectively. The parameter 'n' signifies the number of photons required to excite electrons from the ground state to a higher energy state. In the conventional one-photon lanthanide-induced DCL, 'n' is defined as 1. Conversely, for the Tm^{3+}-induced UCL process, 'n' is defined as 2, corresponding to a two-photon process. Consequently, a local electric field enhancement by a factor of up to 5 can accelerate the excitation rate of Tm^{3+} ions by a maximum of 625-fold theoretically.

In the absence of other interactions, the NIR-UCL intensity from Tm^{3+} doped UCNPs under 1208 nm excitation can be enhanced by up to 625-fold. However, the competitive radiative and non-radiative decay rates of Tm^{3+} induced 'one-photon' DCL, such as transitions of ($^3H_5 \longrightarrow {}^3H_6$, $^3F_4 \longrightarrow {}^3H_6$) of Tm^{3+} may also be enhanced by plasmonic characteristics of Ag-HCNA. This enhancement can lead to faster depopulation of $^3H_5$ states, thereby supressing UCL processes.

In addition to accelerating the excitation rate, the emission rate of UCNPs can be increased when they are positioned near metallic arrays. This enhancement arises from the acceleration of the radiative decay rate of excited states via the Purcell effect through plasmonic confinement. Such an increase in the emission rate significantly contributes to the overall fluorescence enhancement. To further

Open Access Article. Published on 13 April 2026. Downloaded on 4/14/2026 3:06:13 PM.
This article is licensed under a Creative Commons Attribution 3.0 Unported Licence.

Nanoscale Accepted Manuscript

View Article Online
DOI: 10.1039/D6NR00068A

understand the role of emission rate enhancement, the fluorescence lifetimes at 808 nm from UCNPs on glass and Ag-HCNAs were measured, shown in Figure 5.

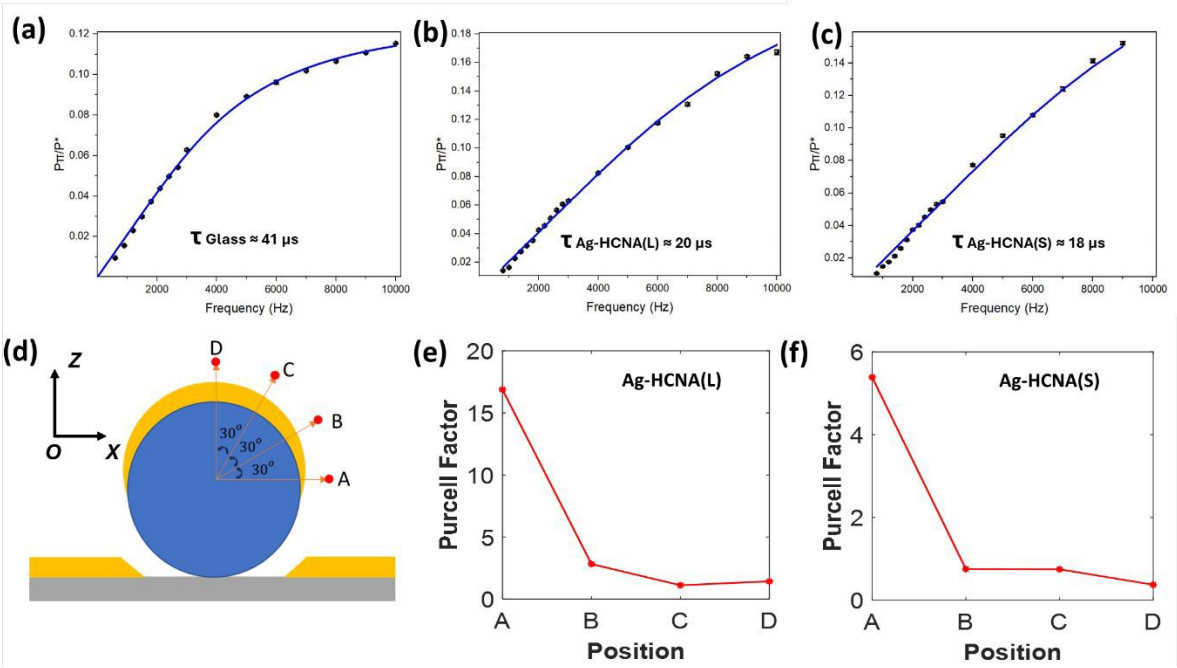

Figure 5 Lifetime measurements and Purcell factor simulations for Tm^{3+} induced NIR-UCL emission at 808 nm under 1208 nm excitation. (a-c) Lifetime plot and mono-exponential fit curve of (a) Tm^{3+} doped UCNPs on glass, (b) Tm^{3+} doped UCNPs on Ag-HCNA(L) film, (c) Tm^{3+} doped DCNPs on Ag-HCNA(S). (d-f) Purcell factor simulations for both types of Ag-HCNA structures. (d) schematic illustrations Purcell factor modelling configuration. (e-f) Averaged Purcell factors versus positions for (e) Ag-HCNA(L) and (f) Ag-HCNA(S).

To analyze the excited-state lifetime of Tm^{3+}, the decay curves presented in Figures 5a–c were obtained using a frequency-domain approach. In each measurement, the samples were excited at 1208 nm, and the emitted photons at 808 nm were collected. Both the excitation and emission beams were directed through mechanical choppers to produce a near-square-wave modulation response. This configuration enables the investigation of the population dynamics of the excited state under periodic excitation. Under square-wave modulation at a frequency ν over a single period $T = \nu^{-1}$, the temporal evolution of the emitting state was interpreted using a three-level model. The spectrometer integrates the signal over an integration time, corresponding to $\nu \cdot t_{int}$ modulation periods. When the two choppers are operated out of phase (blocking the emission while the sample is excited, and vice versa), the measured signal, denoted P_π, reflects the delayed emission dynamics. This signal is normalized against a reference measurement $P_* = \eta \cdot t_{int}$, obtained under identical integration conditions but without the choppers, where η represents the overall collection and detection efficiency. The ratio P_π/P_* is plotted as a function of modulation frequency on the y-axis in Figure 5a–c. By analyzing the frequency-dependent behaviour of this ratio using Equations 1-6 from the

Open Access Article. Published on 13 April 2026. Downloaded on 4/14/2026 3:06:13 PM.
This article is licensed under a Creative Commons Attribution 3.0 Unported Licence.

Nanoscale Accepted Manuscript

View Article Online
DOI: 10.1039/D6NR00068A

Supplementary Document, the excited-state lifetime of Tm^{3+} can be extracted, as the roll-off in the normalized signal with increasing frequency reflects the finite response time of the emitting state.

The measurement reveals that UCNPs on glass exhibit an intrinsically longer lifetime of ~41 µs, whereas UCNPs on Ag-HCNA(S) and Ag-HCNA(L) exhibit significantly shorter lifetimes of ~18 µs and 20 µs, respectively. Previous studies have shown that the fluorescence lifetime of lanthanide ions in a plasmonic cavity can be decomposed into two distinct emitter lifetimes, equivalent to a bi-exponential fit. In such cases, the longer lifetime is associated with uncoupled emitting ions, while the shorter lifetime corresponded to plasmonic-coupled ions [28],[29],[40]. However, in this study, UCNPs coupled with both types of Ag-HCNAs exhibit fluorescence lifetimes that can only be modelled using a mono-exponential fit, indicating uniformly shorter lifetimes. This observation can be attributed to the predominance of photons with faster decay rates, overshadowing those with longer decay rates that remain unaffected by the plasmonic effect. Consequently, the detection of photons with longer decay rates becomes negligible compared to the substantial number of photons with shorter decay rates.

When coupled with metallic arrays, both the radiative and non-radiative decay rates of Tm^{3+} ions can be increase. The increase in the radiative decay rate directly contributes to the enhanced fluorescence. However, a concurrent rise in the non-radiative decay rate leads to fluorescence quenching. Notably, by pre-coating a dielectric spacer layer ~5 nm thick over the surface of the Ag-HCNA, the non-radiative decay rate can be significantly reduced[28]. Therefore, the spacer layer enabled a net emission enhancement of NIR-I UCL while minimizing increase of the non-radiative decay rate.

Based on Supplementary Figure 4, it is assumed that multi-layer Tm^{3+}-doped UCNPs are uniformly deposited on both Ag-HCNA(L) and Ag-HCNA(S), forming a ~70 nm thick layer of DCNPs, which corresponds to approximately three layers of UCNPs. Given that UCNPs are situated in regions with varying degrees of E-field enhancement, it can be inferred from Supplementary Figure 4a and 4b that ~25% of the total UCNPs on Ag-HCNA(S) experienced a local E-field enhancement ranging from 2-fold to 5-fold, while the remaining 75% experience negligible E-field enhancement. For UCNPs on Ag-HCNA(L), it was estimated that only 15% of the total UCNPs experience a local E-field enhancement within the same range, with 85% experiencing negligible enhancement. Among the UCNPs subjected to enhanced E-fields, the majority were within regions experiencing an ~2.5 to 3-fold enhancement.

Assuming an average local E-field enhancement of 2.5-fold and using the measured lifetimes of pristine UCNPs and plasmonic-modified UCNPs, the radiative decay rate enhancement was estimated to be ~5.4-fold for UCNPs on Ag-HCNA(S) and ~4.4-fold for UCNPs on Ag-HCNA(L). Correspondingly, applying Equations 8–13 from the Supplementary Document yields an estimated quantum yield enhancement of approximately 2.3-fold for UCNPs on Ag-HCNA(S) and 2.1-fold for those on Ag-

Open Access Article. Published on 13 April 2026. Downloaded on 4/14/2026 3:06:13 PM.
This article is licensed under a Creative Commons Attribution 3.0 Unported Licence.

Nanoscale Accepted Manuscript

View Article Online
DOI: 10.1039/D6NR00068A

HCNA(L). When considering an average local E-field enhancement of 3-fold, the radiative decay rate enhancement was estimated to be approximately 2.6-fold for UCNPs on Ag-HCNA(S) and 2.1-fold for UCNPs on Ag-HCNA(L), with negligible changes in the corresponding quantum yield enhancement. Under these assumptions, the valid range for the quantum yield enhancement was between 1.1 and 2.3 for UCNPs on Ag-HCNA(S), and between 1 and 2.1 for UCNPs on Ag-HCNA(L). These results suggest that local E-field enhancement, which accelerates 'two-photon' excitation processes, plays a primary role in enhancing the overall UCL signals from Tm^{3+}-doped UCNPs.

In Figure 5d-f, the simulated Purcell factor for emitters situated close to the surfaces of both Ag-HCNA structures is illustrated. It is particularly noteworthy that the Purcell factor is higher near the edge of the Ag hemisphere cap, with the Ag-HCNA(S) structure demonstrating a substantially larger Purcell factor compared to the Ag-HCNA(L). Besides, the average Purcell factors across 4 selected regions are all higher for Ag-HCNA(S) compared to Ag-HCNA(L). This observation aligns well with the radiative decay rate enhancement of Tm-doped UCNPs on both types of Ag-HCNA, as detailed in Table S2. In practice, the measured Purcell factor represents an average value for emitters distributed across all surfaces of the structures, falling within the range of simulated values.

Model System for MEF-Based Immunoassays

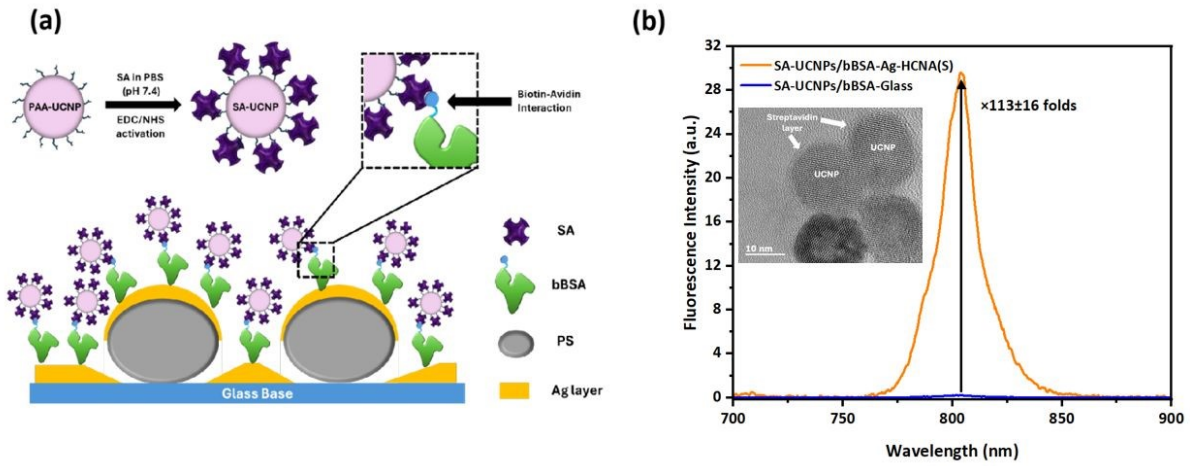

Figure 6 fluorescence enhancement study of a sub-monolayer of SA-UCNPs immobilized onto Ag-HCNA(S). (a) Scheme of sub-monolayer SA-UCNPs coating on Ag-HCNA substrate. (b) fluorescence enhancement test using NIR-II excitation at 1208 nm. Inset: TEM morphological image of SA-UCNPs.

In a practical MEF immunoassay nanoplatform, it is crucial for antibody-labelled fluorescent probes to establish a robust attachment to the protein-anchored plasmonic substrate via a self-assembled monolayer of molecular spacers, even after multiple washing steps [41],[52]. The enhancement of UCL signals using Ag-HCNAs for potential applications in fluorescence immunoassays was further validated

Open Access Article. Published on 13 April 2026. Downloaded on 4/14/2026 3:06:13 PM.
This article is licensed under a Creative Commons Attribution 3.0 Unported Licence.

Nanoscale Accepted Manuscript

View Article Online
DOI: 10.1039/D6NR00068A

and is schematically illustrated in Figure 6a. This study investigates the plasmonic effects of Ag-HCNA film on a sub-monolayer of streptavidin-functionalized Tm^{3+} doped UCNPs immobilized through biotin-streptavidin interactions. A monolayer of bBSA was covalently bound to Ag-HCNAs due to the affinity between silver from the array film and the thiol groups from bBSA. Streptavidin was coated onto individual PAA-UCNPs via EDC-NHS chemistry, leveraging the interaction between carboxyl groups from PAA and amino groups from streptavidin. Subsequently, streptavidin-functionalized UCNPs were firmly immobilized on bBSA-coated Ag-HCNAs through biotin-avidin interactions, remaining stable even after multiple wash cycles. Figure 6b inset shows individual UCNPs surrounded by an amorphous layer, confirming successful streptavidin functionalization. PL spectra in Figure 6b reveal that the near-infrared UCL signals from a sub-monolayer of UCNPs immobilized on glass are exceedingly weak, while UCNPs immobilized on Ag-HCNAs exhibit a pronounced UCL signal, with an average enhancement of 113-fold compared to UCNPs on glass. These preliminary results validate the potential of significantly amplifying weak NIR-UCL signals from sub-monolayer UCNPs, which contain a much lower concentration of UCNPs compared to multi-layer configurations. For practical ELISA measurements, we aim to continually improve the limit of detection by measuring fluorescence signals from UCNP concentrations as low as pg/L. With Ag-HCNAs serving as signal amplifiers, we are confident in achieving this objective.

Conclusion

This study presents a significant advancement in utilizing plasmonic-enhanced NIR-II responsive UCNPs. By coupling Tm^{3+}-doped $NaYF_4$ UCNPs with PEGylated Ag-HCNA through drop-casting, a substantial enhancement of more than 240-fold was observed in Tm^{3+}-induced UCL at 808 nm under 1208 nm laser excitation, compared to pristine UCNPs on glass substrates. The underlying enhancement mechanisms were investigated using 3D-FDTD simulations at 1208 nm excitation, which revealed localised electromagnetic 'hot spots' at the edges of hemispherical caps. Lifetime measurements further indicated that the dominant contribution to the observed UCL enhancement arises from local electric field amplification, which exhibits a quadratic dependence on the excitation power. In contrast, the contribution of emission enhancement plays a secondary role. Moreover, the potential of Ag-HCNA-based UCL amplification for fluorescence immunoassay applications was validated by immobilizing a sub-monolayer of streptavidin-functionalized UCNPs on biotinylated bovine serum albumin (bBSA) pre-grafted array substrates. A remarkable enhancement up to 113-fold relative to traditional glass substrates was achieved, demonstrating the capability of this approach to substantially amplify weak NIR-UCL signals in plasmonic-enhanced UCL immunoassay platforms. The designed plasmonic-enhanced UCL platform, featuring excitation within the biologically transparent

Open Access Article. Published on 13 April 2026. Downloaded on 4/14/2026 3:06:13 PM.
This article is licensed under a Creative Commons Attribution 3.0 Unported Licence.

Nanoscale Accepted Manuscript

View Article Online
DOI: 10.1039/D6NR00068A

NIR-II window and emission in the NIR-I region, offers distinct technical and economic advantages. These include reduced biological autofluorescence, improved signal-to-noise performance and cost-effective detection of NIR-I emission using conventional silicon-based detectors. In summary, the integration of NIR-I emitting UCNPs with plasmonic nanoarrays provides a powerful and practical sensing platform with strong potential to advance the field of fluorescence-based immunoassays technologies.

Open Access Article. Published on 13 April 2026. Downloaded on 4/14/2026 3:06:13 PM.
This article is licensed under a Creative Commons Attribution 3.0 Unported Licence.

Data Availability Statements

The data that support the findings of this study are available from the corresponding author upon reasonable request.

Author Declarations

Conflict of Interest

The authors have no conflicts to disclose.

Reference

1. Fothergill, S.M., C. Joyce, and F. Xie, *Metal enhanced fluorescence biosensing: From ultra-violet towards second near-infrared window.* Nanoscale, 2018. **10**(45): p. 20914-20929.
2. Li, M., et al., *Light - activated nanoprobes for biosensing and imaging.* Advanced Materials, 2019. **31**(45): p. 1804745.
3. Hang, Y., J. Boryczka, and N. Wu, *Visible-light and near-infrared fluorescence and surface-enhanced Raman scattering point-of-care sensing and bio-imaging: A review.* Chemical Society Reviews, 2022. **51**(1): p. 329-375.
4. Martins, I.S., et al., *Measurement of tissue optical properties in a wide spectral range: a review.* Biomedical Optics Express, 2022. **14**(1): p. 249-298.

Nanoscale Accepted Manuscript

View Article Online
DOI: 10.1039/D0NR00068A

5. Tuchin, V.V., *Tissue optics and photonics: light-tissue interaction.* Journal of Biomedical Photonics & Engineering, 2015. **1**(2): p. 98-134.
6. Chen, C., et al., *Activatable fluorescence probes for "turn-on" and ratiometric biosensing and bioimaging: from NIR-I to NIR-II.* Bioconjugate Chemistry, 2020. **31**(2): p. 276-292.
7. Li, S., et al., *Recent progresses in NIR-I/II fluorescence imaging for surgical navigation.* Frontiers in Bioengineering and Biotechnology, 2021. **9**: p. 768698.
8. Lei, Z. and F. Zhang, *Molecular engineering of NIR - II fluorophores for improved biomedical detection.* Angewandte Chemie International Edition, 2021. **60**(30): p. 16294-16308.
9. Cao, J., et al., *Recent progress in NIR-II contrast agent for biological imaging.* Frontiers in bioengineering and biotechnology, 2020. **7**: p. 487.
10. Antaris, A.L., et al., *A small-molecule dye for NIR-II imaging.* Nature materials, 2016. **15**(2): p. 235-242.
11. Li, L., et al., *A short review on NIR-II organic small molecule dyes.* Dyes and Pigments, 2020. **183**: p. 108756.
12. Chen, L.L., et al., *Near - infrared - II quantum dots for in vivo imaging and cancer therapy.* Small, 2022. **18**(8): p. 2104567.
13. Xu, S., J. Cui, and L. Wang, *Recent developments of low-toxicity NIR II quantum dots for sensing and bioimaging.* TrAC Trends in Analytical Chemistry, 2016. **80**: p. 149-155.
14. Pan, J., F. Li, and J.H. Choi, *Single-walled carbon nanotubes as optical probes for bio-sensing and imaging.* Journal of Materials Chemistry B, 2017. **5**(32): p. 6511-6522.
15. Hong, G. and H. Dai, *In vivo fluorescence imaging in the second near-infrared window using carbon nanotubes.* In Vivo Fluorescence Imaging: Methods and Protocols, 2016: p. 167-181.
16. Ding, S., et al., *Recent progress in NIR-II emitting lanthanide-based nanoparticles and their biological applications.* Journal of rare earths, 2020. **38**(5): p. 451-463.
17. Ge, X., R. Wei, and L. Sun, *Lanthanide nanoparticles with efficient near-infrared-II emission for biological applications.* Journal of Materials Chemistry B, 2020. **8**(45): p. 10257-10270.
18. Yi, Z., et al., *Lanthanide-activated nanoparticles: a toolbox for bioimaging, therapeutics, and neuromodulation.* Accounts of Chemical Research, 2020. **53**(11): p. 2692-2704.

Open Access Article. Published on 13 April 2026. Downloaded on 4/14/2026 3:06:13 PM.
This article is licensed under a Creative Commons Attribution 3.0 Unported Licence.

Nanoscale Accepted Manuscript

View Article Online
DOI: 10.1039/D0NR00068A

19. Liu, Y., K. Ai, and L. Lu, *Designing lanthanide-doped nanocrystals with both up-and down-conversion luminescence for anti-counterfeiting.* Nanoscale, 2011. **3**(11): p. 4804-4810.

20. Nadort, A., J. Zhao, and E.M. Goldys, *Lanthanide upconversion luminescence at the nanoscale: fundamentals and optical properties.* Nanoscale, 2016. **8**(27): p. 13099-13130.

21. DaCosta, M.V., et al., *Lanthanide upconversion nanoparticles and applications in bioassays and bioimaging: A review.* Analytica chimica acta, 2014. **832**: p. 1-33.

22. Yan, J., et al., *Progress in light-responsive lanthanide nanoparticles toward deep tumor theranostics.* Advanced Functional Materials, 2021. **31**(42): p. 2104325.

23. Wang, F., R. Deng, and X. Liu, *Preparation of core-shell NaGdF4 nanoparticles doped with luminescent lanthanide ions to be used as upconversion-based probes.* Nature protocols, 2014. **9**(7): p. 1634-1644.

24. Lei, X., et al., *Intense near-infrared-II luminescence from NaCeF 4: Er/Yb nanoprobes for in vitro bioassay and in vivo bioimaging.* Chemical science, 2018. **9**(20): p. 4682-4688.

25. Song, Y., et al., *Deep learning fluorescence imaging of visible to NIR-II based on modulated multimode emissions lanthanide nanocrystals.* Advanced Functional Materials, 2022. **32**(45): p. 2206802.

26. Ansari, A.A., et al., *Luminescent lanthanide nanocomposites in thermometry: Chemistry of dopant ions and host matrices.* Coordination Chemistry Reviews, 2021. **444**: p. 214040.

27. Yang, H., et al., *Preparation and properties of Nd3+ doped Gd2O3 near-infrared phosphor.* Ceramics International, 2021. **47**(6): p. 8510-8517.

28. Xu, J., et al., *Plasmonic-Enhanced NIR-II Downconversion Fluorescence beyond 1500 nm from Core–Shell–Shell Lanthanide Nanoparticles.* Advanced Optical Materials, 2023. **11**(19): p. 2300477.

29. Xu, J., et al., *Remarkable Plasmonic Enhanced Luminescence of Ce3+ doped Lanthanide Downconversion Nanoparticles in NIR-II Window by Silver Hole-Cap Nanoarrays.* Advanced Optical Materials, 2024. **12**(30): p. 2400660.

30. Bi, S., et al., *NIR-II Responsive Upconversion Nanoprobe with Simultaneously Enhanced Single-Band Red Luminescence and Phase/Size Control for Bioimaging and Photodynamic Therapy.* Advanced Materials, 2023. **35**(7): p. 2207038.

Open Access Article. Published on 13 April 2026. Downloaded on 4/14/2026 3:06:13 PM.
This article is licensed under a Creative Commons Attribution 3.0 Unported Licence.

Nanoscale Accepted Manuscript

View Article Online
DOI: 10.1039/D0SR00068A

31. Li, Y., et al., *Engineered lanthanide-doped upconversion nanoparticles for biosensing and bioimaging application.* Microchimica Acta, 2022. **189**(3): p. 109.
32. Guo, Y., et al., *In vivo NIR-II fluorescence lifetime imaging of whole-body vascular using high quantum yield lanthanide-doped nanoparticles.* Small, 2023. **19**(35): p. 2300392.
33. Smith, A.M., M.C. Mancini, and S. Nie, *Second window for in vivo imaging.* Nature nanotechnology, 2009. **4**(11): p. 710-711.
34. Derom, S., et al., *Metal enhanced fluorescence in rare earth doped plasmonic core–shell nanoparticles.* Nanotechnology, 2013. **24**(49): p. 495704.
35. Aslan, K., et al., *Metal-enhanced fluorescence: an emerging tool in biotechnology.* Current opinion in biotechnology, 2005. **16**(1): p. 55-62.
36. Saboktakin, M., et al., *Metal-enhanced upconversion luminescence tunable through metal nanoparticle–nanophosphor separation.* ACS nano, 2012. **6**(10): p. 8758-8766.
37. Jeong, Y., et al., *Metal enhanced fluorescence (MEF) for biosensors: General approaches and a review of recent developments.* Biosensors and Bioelectronics, 2018. **111**: p. 102-116.
38. Dhanasiwawong, K., et al., *Preparation of 2D Periodic Nanopatterned Arrays through Vertical Vibration-Assisted Convective Deposition for Application in Metal-Enhanced Fluorescence.* Processes, 2022. **10**(2): p. 202.
39. Saboktakin, M., et al., *Plasmonic enhancement of nanophosphor upconversion luminescence in Au nanohole arrays.* ACS nano, 2013. **7**(8): p. 7186-7192.
40. Xie, F., et al., *Nanoscale control of Ag nanostructures for plasmonic fluorescence enhancement of near-infrared dyes.* Nano Research, 2013. **6**: p. 496-510.
41. Li, Y., et al., *NIR-II emitting rare-earth nanoparticles for a lateral flow immunoassay in hemolysis.* Sensors and Actuators B: Chemical, 2021. **345**: p. 130380.
42. Song, Z., et al., *NIR-II fluorescent nanoprobe-labeled lateral flow biosensing platform: A high-performance point-of-care testing for carcinoembryonic antigen.* Biosensors and Bioelectronics, 2023. **224**: p. 115063.
43. Song, Z., et al., *NIR-II fluorescence lateral flow immunosensor based on efficient energy transfer probe for point-of-care testing of tumor biomarkers.* Chinese Chemical Letters, 2024: p. 109834.
44. Kong, W., et al., *A general strategy for ligand exchange on upconversion nanoparticles.* Inorganic Chemistry, 2017. **56**(2): p. 872-877.

Open Access Article. Published on 13 April 2026. Downloaded on 4/14/2026 3:06:13 PM.
This article is licensed under a Creative Commons Attribution 3.0 Unported Licence.

Nanoscale Accepted Manuscript

View Article Online
DOI: 10.1039/D0NR00068A

45. Theodorou, I., et al., *Significant metal enhanced fluorescence of Ag 2 S quantum dots in the second near-infrared window.* Nanoscale, 2016. **8**(26): p. 12869-12873.

46. Pang, J.S., et al., *Tunable three-dimensional plasmonic arrays for large near-infrared fluorescence enhancement.* ACS applied materials & interfaces, 2019. **11**(26): p. 23083-23092.

47. Pang, J., et al., *Gold nanodisc arrays as near infrared metal-enhanced fluorescence platforms with tuneable enhancement factors.* Journal of Materials Chemistry C, 2017. **5**(4): p. 917-925.

48. Xu, J., et al., *Significant quantum yield enhancement for near infrared fluorescence dyes by silica templated silver nanorods.* Applied Physics Reviews, 2022. **9**(3).

49. Güsken, N.A., et al., *Emission enhancement of erbium in a reverse nanofocusing waveguide.* Nature Communications, 2023. **14**(1): p. 2719.

50. Darvill, D., et al., *Breaking the symmetry of nanosphere lithography with anisotropic plasma etching induced by temperature gradients.* Nanoscale Advances, 2021. **3**(2): p. 359-369.

51. Wu, D.M., et al., *Plasmon-enhanced upconversion.* The journal of physical chemistry letters, 2014. **5**(22): p. 4020-4031.

52. Chen, R., et al., *NIR-II emissive lateral flow immunoassay for accurate determination of tumor marker in hemolysis.* Sensors and Actuators B: Chemical, 2021. **328**: p. 129050.

Open Access Article. Published on 13 April 2026. Downloaded on 4/14/2026 3:06:13 PM.
This article is licensed under a Creative Commons Attribution 3.0 Unported Licence.

Nanoscale Accepted Manuscript

View Article Online
DOI: 10.1039/D6NR00068A

The authors confirm that the data supporting the findings of this study are available within the article and its supplementary materials.

Open Access Article. Published on 13 April 2026. Downloaded on 4/14/2026 3:06:13 PM.
This article is licensed under a Creative Commons Attribution 3.0 Unported Licence.

Nanoscale Accepted Manuscript